Eccentricity of the geomagnetic dipole caused by lopsided inner core growth

Peter Olson* and Renaud Deguen

Seismic images of Earth's inner core reveal an east–west dichotomy[1-3]. This dichotomy has been interpreted as lopsided growth, with faster solidification on one hemisphere of the inner core boundary, and slower solidification and perhaps melting on the other[4,5]. Today, the geomagnetic field that originates in the core is also slightly lopsided, with reconstructions revealing an offset of the dipole axis from Earth's centre by more than 500 km. The geomagnetic dipole has moved into Earth's Eastern Hemisphere over the past two centuries[6,7] and has declined in intensity[8]. However, reconstructions of the magnetic field from the past 10,000 years[9,10] show that the dipole previously had an offset to the west and reconstructions of the older palaeomagnetic field[11,12] yield a dipole with an offset to the east. Here we use numerical simulations of the dynamo to show that lopsided inner core growth can cause persistent eccentricity of the geomagnetic field, with the best-fitting dipole axis offset in the direction of fastest inner core solidification. Our results therefore imply that faster growth may have occurred in the Western Hemisphere of the inner core during the past ten millennia. In contrast, offset of the palaeomagnetic dipole implies faster Eastern Hemisphere growth at earlier times. We suggest that a reorientation of the location of fastest inner core growth has occurred over the past 5 million years.

According to dynamo theory, the time-average geomagnetic field in the core should be highly symmetric because of the strong dynamical constraints of Earth's rotation[13]. Figure 1 shows, however, that the geomagnetic field in the core has been eccentric for at least 10,000 years, with the axis of the best-fitting dipole offset from Earth's centre by several hundred kilometres. Persistent dipole offset in one direction can be produced by lateral heterogeneity in the core with an azimuthal mode $m = 1$ pattern of longitude variation. Seismically measurable heterogeneity of this type in the liquid outer core is considered unlikely[14] and indeed none has been detected[15]. The solid lower mantle has substantial lateral heterogeneity that affects the geodynamo, but its seismic structure has a dominant mode $m = 2$ pattern of longitude variation[16] and minimal $m = 1$ variation. In contrast, the structure of the solid inner core is highly eccentric by virtue of its east–west dichotomy. Inner core solidification releases buoyant light elements such as S, Si and O (ref. 17) into the iron-rich outer core[18] and lopsided inner core growth is expected to produce an $m = 1$ contribution to the pattern of convection in the outer core, a possible source for the observed geomagnetic eccentricity. The inner core may align with the mantle heterogeneity, but the evidence is inconclusive as to which side of the inner core grows fastest[19-21], so both possibilities must be considered.

We calculate the magnetic eccentricity produced by inner core boundary (ICB) heterogeneity and by core–mantle boundary (CMB) heterogeneity using numerical dynamos driven by
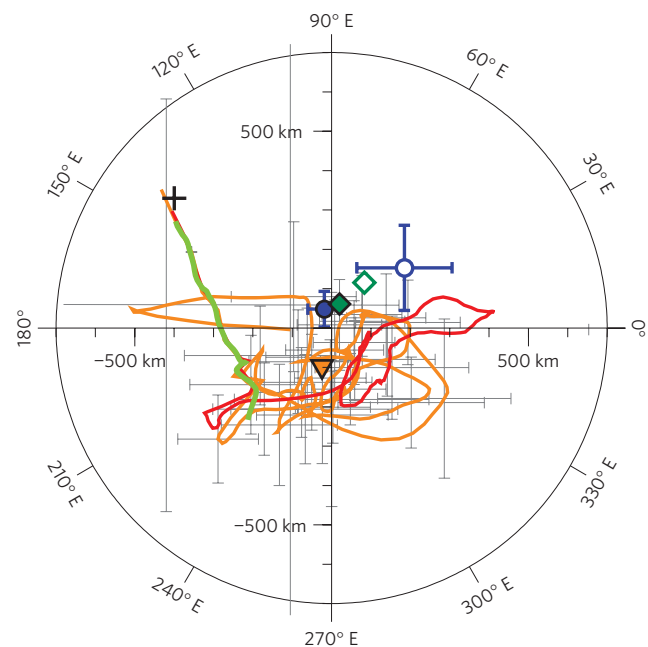

Figure 1 | Geomagnetic dipole eccentricity. Best-fitting geomagnetic dipole axis locations in the equatorial plane of the core relative to Earth's centre determined using the method of ref. 27, in light green for years 1590–1990 from historical field model gufm1 (ref. 28), in red for 0–3,000 years ago from archaeomagnetic field model CALS3k.4b (ref. 9) and in orange for 0–10,000 years ago from archaeomagnetic field model CALS10k.1b (ref. 10) with uncertainties (± one standard deviation) at every ten data points shown in light grey. The orange triangle is the time-average location of the dipole axis from CALS10k.1b. Also shown are time-average dipole axis locations for 0–5 Myr ago from palaeomagnetic field reconstructions in ref. 11 (green diamonds) and ref. 12 (blue symbols with error bars, showing the uncertainties on the mean dipole axis location). Filled and open symbols indicate normal and reverse polarity times, respectively. The black cross shows the dipole axis location at epoch 2009 from geomagnetic field model GRIMM-2 (ref. 29).

convection, with buoyancy in the outer core represented in terms of co-density, a linear combination of temperature and light-element concentration. Figure 2 shows the core structure of four dynamos with different ICB and CMB conditions that are otherwise identical in terms of their control parameters. The dynamo in Fig. 2a includes a hemispherically asymmetric ICB with an $m = 1$ longitude variation in co-density oriented to produce a greater release of buoyancy on the western side of the inner core and a homogeneous CMB. The dynamo in Fig. 2b includes heat-flow variations on the CMB
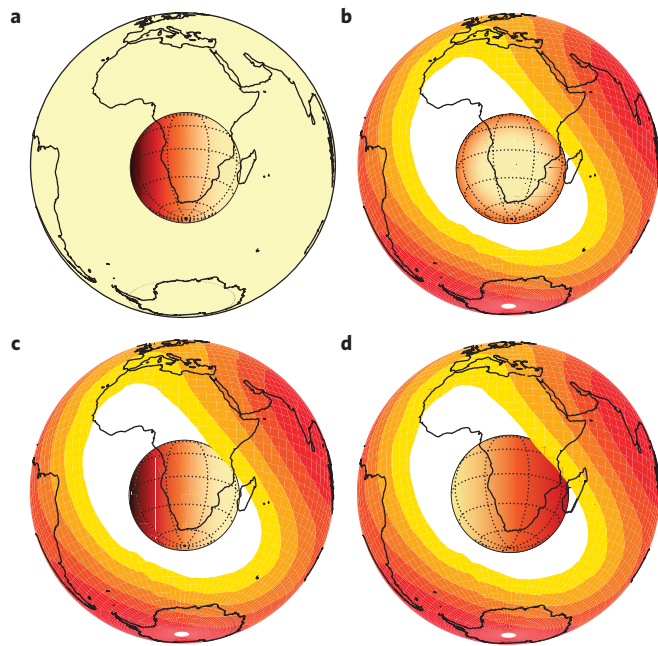
Department of Earth and Planetary Sciences, Johns Hopkins University, Baltimore, Maryland 21218, USA. *e-mail: olson@jhu.edu.

Figure 2 | Dynamo boundary heterogeneity. Dynamo **a**, uniform CMB (core–mantle boundary) heat flow and higher buoyancy (that is, faster growth rate) on the west side of the ICB (inner core boundary); **b**, non-uniform CMB heat flow (red = high; white = low) and uniform ICB; **c**, non-uniform CMB heat flow and higher buoyancy on the west side of the ICB; **d**, non-uniform CMB heat flow and higher buoyancy on the east side of the ICB. Continental outlines are shown on the CMB for reference.

Figure 3 | Dynamo eccentricity. a–d, Scatter of the best-fitting dipole axis locations in the equatorial plane of the core relative to Earth's centre over 25 dipole decay times (approximately 500,000 years in the core) from the four dynamos in Fig. 2. The ICB (radius 1,220 km) is shown by dashed circles. Blue crosses and blue circles show the time-average locations of the dipole axes and one standard deviation, respectively.

that are proportional to the long-wavelength variations in seismic shear-wave velocity in the lower mantle, with higher than average CMB heat flow in regions with higher than average lower-mantle seismic velocity and a homogeneous ICB. The dynamo in Fig. 2c includes the same CMB heat-flow heterogeneity as Fig. 2b and the same as ICB heterogeneity as Fig. 2a, whereas the dynamo in Fig. 2d is the same as Fig. 2c except that the orientation of the ICB heterogeneity is rotated by 180°, producing greater buoyancy release on the eastern side. Details of numerical dynamos and their scaling to the core are described in the Methods.

Figure 3 shows the scatter of best-fitting dipole axis locations in the equatorial plane for these four dynamos. The average dipole location in Fig. 3a is offset from Earth's centre by 550 km along longitude 110° W, approximately 20° to the west of the direction corresponding to the fastest inner core solidification, and its dipole axis is largely confined to the Western Hemisphere of the core. The few times when the dipole axis wanders far into the Eastern Hemisphere correspond to dipole collapse events, often accompanied by polarity reversals. In contrast, the dipole axis locations in Fig. 3b are nearly symmetric about Earth's centre, demonstrating that CMB heat-flow heterogeneity with a dominant $m = 2$ pattern fails to localize the dipole eccentricity in one hemisphere. The scatter of dipole axis locations and the mean dipole location for Fig. 3c are more similar to Fig. 3a than b, demonstrating that lopsided inner core growth is stronger than CMB heterogeneity in controlling the dipole eccentricity. Figure 3d demonstrates that rotating the ICB heterogeneity also rotates the dipole eccentricity. There is more scatter in the dipole locations in Fig. 3d compared with c, the difference attributable to small amounts of $m = 1$ and $m = 3$ heterogeneity in the CMB heat flux. In the Supplementary Information we show that for otherwise similar dynamos with uniform conditions at the ICB and CMB the average dipole location coincides with Earth's centre, whereas the scatter tends to increase with the convective forcing and decrease with the rate of rotation.
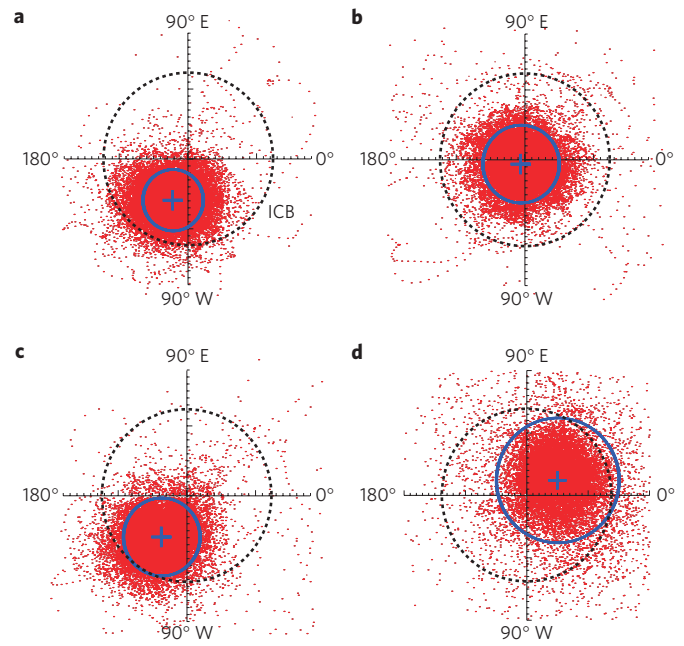
Figure 4 shows time-average structure of the four dynamos, including the radial magnetic-field intensity at the CMB and the distribution of co-density in the equatorial plane of the outer core. Figure 4a shows an observable signature of lopsided inner core growth. The westward offset of the dipole axis relative to the rotation axis in this case produces one high-intensity flux concentration in each of the Northern and Southern hemispheres centred near longitude 100° W, in the general direction of fastest inner core growth. The time-average magnetic field consists of an axial dipole plus significant contributions from non-axial quadrupole terms with $m = 1$. Figure 4b shows the influence of lower-mantle heterogeneity on the dynamo structure. In this case the time-average magnetic field on the CMB is not axisymmetric and includes high-latitude, high-intensity magnetic-field concentrations particularly in the Northern Hemisphere at the approximate longitudes where the CMB heat flow is highest. The time-average magnetic field is also somewhat different in the Northern and Southern hemispheres because of deviations from north–south symmetry in the lower-mantle seismic structure, nevertheless it is predominantly an axial dipole with contributions from a few other spherical harmonics, most notably the non-axial quadrupole terms with $m = 2$. Comparable asymmetries are observed in the historical geomagnetic field[22] and are also present in some reconstructions of the palaeomagnetic field for the past[11,12] 5 million years (Myr). Figure 4c,d shows that the combination of lopsided inner core growth aligned with the dominant $m = 2$ lower-mantle structure produces a time-average magnetic field that is basically a superposition of the structures in dynamos a and b, with the magnetic-field structure offset in the direction of fastest inner core growth.

Figure 4 also shows the time-average co-density in the equatorial plane of the outer core for the four dynamos. Because most of the co-density variations are produced by light-element release at the ICB in our dynamos, these plots essentially show the relative concentration of light elements in the outer core. The light-element
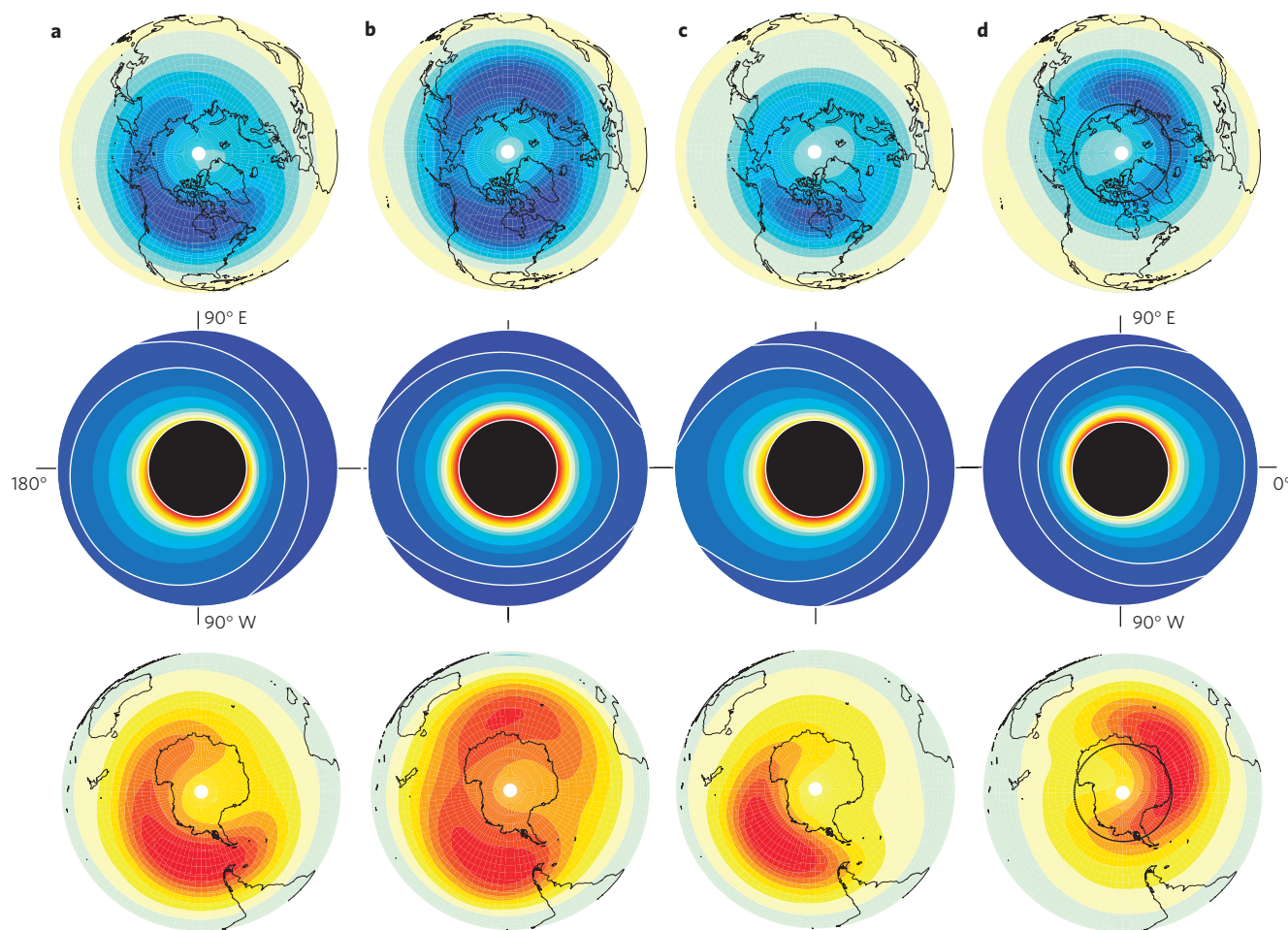
Figure 4 | Eccentric dynamo internal structure. a–d, Structure of the four dynamos in Fig. 2 averaged over 25 dipole decay times. Top and bottom rows: radial component of the magnetic field on the CMB in the Northern and Southern hemispheres, respectively, with continental outlines (black) and rotation axis (white) shown for reference. Blue, negative (radially inward); yellow and red, positive (radially outward) magnetic field. Middle row: buoyancy distribution representing the light-element concentration in the equatorial plane of the outer core for the same dynamos with the inner core shown in black. Red, high; blue, low concentrations of light elements; white contours for emphasis. Orientations are the same in all three rows, with 90° E at the top and 90° W at the bottom of each image.

concentration in Fig. 4a is circular and eccentric, in Fig. 4b it is elliptical and concentric, and in Fig. 4c,d it is elliptical and eccentric, with an offset in the same quadrant as the dipole axis. We note that these lateral variations in co-density are substantial in our numerical dynamos, but when scaled to outer core conditions they would be below the limit of seismic detection.

The outer core flow in these dynamos is a superposition of a generally westward-directed azimuthal flow superimposed on columnar convection, producing intense vortices that drift westwards in the equatorial plane. Magnetic field in the equatorial plane is concentrated within the columns that have anticyclonic vorticity. With homogeneous boundary conditions, the westward-drifting vortices average out the longitudinal heterogeneity, so the best-fitting dipole coincides with Earth's rotation axis in time average. With lopsided inner core growth, however, the vorticity in the columnar convection is strongest in the hemisphere where the light-element flux is highest, so the average magnetic field is slightly stronger there, displacing the dipole axis in that direction. Because the CMB heterogeneity is dominated by an $m = 2$ pattern, it produces two sectors with enhanced vorticity nearly 180° apart in longitude, which does not localize the dipole offset.

Figure 5 shows the distribution of dipole axis locations from the lopsided ICB dynamo a spanning a dipole collapse event that resulted in a reverse-to-normal polarity change. The time interval spans four dipole decay times, approximately 80,000 years in the core. During the stable reverse polarity time (blue dots in Fig. 5) the dipole intensity is high, the dipole offset is relatively small and the dipole axis is confined to the Western Hemisphere of the core. This situation changes at the onset of the reversal. As the dipole intensity diminishes and the field assumes a transitional multipolar structure (red dots in Fig. 5), the dipole axis drifts far into the Eastern Hemisphere. Following the polarity change the dipole intensity recovers, the new (normal) polarity stabilizes, the dipole axis returns to the Western Hemisphere (green dots in Fig. 5) and the scatter of dipole axis locations reverts to that before the reversal.

Our results reveal a close connection between persistent dipole eccentricity and mode $m = 1$ lateral heterogeneity in the core and offer an explanation for the dominantly westward offset of the geomagnetic dipole axis over the past 10,000 years in terms of lopsided inner core growth. In the past two centuries the geomagnetic dipole axis has behaved differently, moving far into the Eastern Hemisphere, coincident with the growth of reversed flux in the South Atlantic region of the CMB and the precipitous decline in the geomagnetic dipole intensity[8]. This is not incompatible with its previous history, however. A previous study[7] attributes the present-day geomagnetic dipole eccentricity to the asymmetric distribution of the high-intensity, high-latitude flux patches in the present-day geomagnetic field on the CMB, the same basic
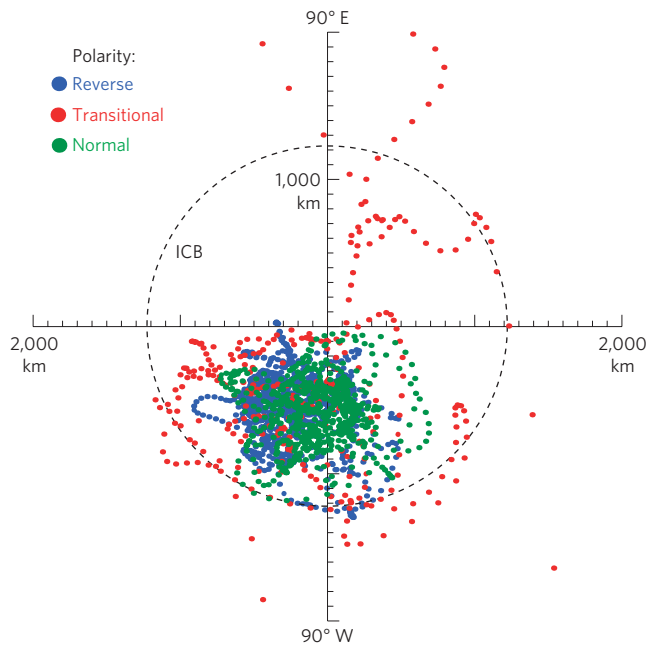
567

Figure 5 | Dipole eccentricity during a reversal. Scatter of the best-fitting dipole axis locations in the equatorial plane of the core relative to Earth's centre before, during and after a reverse-to-normal magnetic polarity change in dynamo a with lopsided inner core growth sampled every 90 years. Blue, reverse polarity (before); red, transitional polarity (during); green, normal polarity (after). The ICB is shown by the dashed circle.

kinematics associated with dipole offset in our dynamos, and the authors further argue that increases in the geomagnetic dipole offset are caused by fluctuations in these high-intensity flux patches. Fluctuations in dipole offset in our dynamos are likewise connected to fluctuations in the high-intensity flux patches and erratic dipole offsets, including hemisphere crossings, typically occur when the dipole intensity decreases, particularly in advance of polarity reversals and excursions. Observations over a much longer time span are needed to determine if recent geomagnetic field behaviour signals this process.

Finally, we note that very long-lived dipole eccentricity would constitute strong evidence for lopsided inner core growth in the past. The palaeofield reconstructions in Fig. 1 show long-lived dipole eccentricity but with dipole axes located in the Eastern Hemisphere, suggesting a reorientation of the direction of fastest growth of the inner core relative to the mantle over the past 5 Myr. Reorientation of dipole eccentricity on millennial timescales could result from intermittent inner core rotation[23], and on much longer timescales from changes in flow in the inner core[5] and the lower mantle[24].

Methods

Dynamo control parameters and boundary conditions. We represent thermochemical convection by combining temperature T and the light element concentration χ into a co-density variable $C = \alpha T + \beta \chi$, where (α, β) are the expansion coefficients for temperature and composition, respectively. Assuming that T and χ have the same diffusivities, adding their transport-diffusion equations yields a single equation for C. Scaling C using the average rate of light element enrichment in the outer core $\dot{\chi}_o$, the Rayleigh number, Ra, for compositional convection is

$$Ra = \beta g_o d^5 \dot{\chi}_o / \kappa \nu^2 \qquad (1)$$

where g_o is gravity at the CMB, $d = r_o - r_i$, r_o and r_i being outer and inner radii, respectively, κ is the diffusivity of C and ν is the kinematic viscosity. We analyse dynamos with Prandtl number $Pr = \nu/\kappa = 1$, magnetic Prandtl number $Pm = \nu/\eta = 20$, where η is magnetic diffusivity, Ekman number $E = \nu/\Omega d^2 = 6 \times 10^{-3}$, where Ω is rotation angular velocity and Rayleigh number $Ra = 2.5 \times 10^4$.

At the CMB we specify the amplitude and the pattern of the heat flux and set the light-element flux to zero. In the Boussinesq approximation, the outer-boundary co-density flux $\partial C/\partial r$ is equivalent to the CMB heat flux q minus the heat flux conducted down the core adiabat. We represent the large-scale planform of CMB heat flux assuming its lateral variations are linearly proportional to the lateral variations in seismic shear-wave velocity in the lower mantle[25], so that

$$\delta q/\overline{q} \propto \delta V_s/\overline{V_s} \qquad (2)$$

where $\overline{V_s}$ and δV_s are the spherical average and the lateral variations of shear-wave velocity and $\overline{q}$ and δq are the spherical average and the lateral variations of q. We assume the pattern of $\delta q(\theta, \phi)$ is proportional to a model[16] of lower-mantle shear-velocity heterogeneity at 200 km above the CMB truncated at spherical harmonic degree and order 3, and we set the mean CMB flux and its variations to $\partial \overline{C}/\partial r = -0.1$ and $|\partial(\delta C)/\partial r| = 0.05$. The ICB condition for C is

$$C(r_i) = \overline{C_i} + \delta C_i \qquad (3)$$

where $\overline{C_i}$ and δC_i are the spherical average and heterogeneity of the ICB co-density. With our scaling, $\dot{\chi}_o$ appears as a volumetric sink term in the co-density equation.

Dynamo numerics and scalings. The numerical dynamos use code MAG (available at www.geodynamics.org) with 31 Chebyshev polynomials and spherical harmonics up to degree and order 32. Our time unit is the e-fold free decay time of a dipole in a uniformly conducting sphere with radius r_o; in the core $\tau = r_o^2/\pi^2\eta \simeq 20,000$ years. We have run our dynamos for 250τ to ensure statistical equilibration.

Dipole eccentricity increases with ICB heterogeneity and decreases with magnetic Reynolds number. The magnetic Reynolds number $Rm \simeq 200$ in our dynamos, whereas $Rm \simeq 1,000$ in the core. We use $|\delta C_i|/\overline{C_i} = 2$, whereas for the translational instability in the core[5] $|\delta C_i|/\overline{C_i} \simeq 10$, so that $|\delta C_i|/Rm\overline{C_i} \simeq 10^{-2}$ in both situations. The Elsasser number based on the CMB dipole field is $\simeq 0.26$ in our dynamos, versus $\simeq 0.056$ for the present-day geomagnetic field. However, it is shown in ref 26 that for convective dynamos

$$B_d^{CMB} = \gamma(\rho_o\mu_o)^{1/2}(g_o\beta R(\dot{\chi}_o - \dot{\chi}_{cr})d^2)^{1/3} \qquad (4)$$

better scales the dipole field strength, where B_d^{CMB} is the time-average root-mean-square geomagnetic dipole field on the CMB in Tesla, μ_o is magnetic permeability, $\dot{\chi}_{cr}$ is the critical rate of light-element increase for convective onset and $\gamma \simeq 0.1$ is a numerically determined coefficient. Assuming $\rho_o = 11$ Mg m^{-3}, $g_o = 10.7$ m s^{-2}, $\beta = 1$, $\mu_o = 4\pi \times 10^{-7}$ H m^{-1}, $d = 2.258 \times 10^6$ m, $R = r_i/r_o = 0.35$ and $\dot{\chi}_o - \dot{\chi}_{cr} = 3 \times 10^{-19}$ s^{-1} in the core, equation (4) predicts $B_d^{CMB} \simeq 0.21$ mT, slightly less than the present root-mean-square CMB geomagnetic dipole intensity of 0.26 mT but comparable to the time-average dipole intensity inferred from palaeomagnetism[11,12].

Dipole eccentricity. Normalized by Earth's mean radius, the geocentric Cartesian coordinates (x_e, y_e, z_e) of the best-fitting dipole are[27]

$$x_e = \frac{L_1 - g_1^1 F}{3m^2}, \quad y_e = \frac{L_2 - h_1^1 F}{3m^2}, \quad z_e = \frac{L_0 - g_1^0 F}{3m^2} \qquad (5)$$

where (g_l^m, h_l^m) are the Gauss coefficients, $m = [(g_1^0)^2 + (g_1^1)^2 + (h_1^1)^2]^{1/2}$ and

$$L_0 = 2g_1^0 g_2^0 + \sqrt{3}(g_1^1 g_2^1 + h_1^1 h_2^1), \quad L_1 = -g_1^1 g_2^0 + \sqrt{3}(g_1^0 g_2^1 + g_1^1 g_2^2 + h_1^1 h_2^2),$$

$$L_2 = -h_1^1 g_2^0 + \sqrt{3}(g_1^0 h_2^1 - h_1^1 g_2^2 + g_1^1 h_2^2), \quad F = \frac{L_0 g_1^0 + L_1 g_1^1 + L_2 h_1^1}{4m^2}$$

References

1. Niu, F. & Wen, L. Hemispherical variations in seismic velocity at the top of the Earth's inner core. *Nature* **410,** 1081–1084 (2001).
2. Sun, X. & Song, X. Tomographic inversion for three-dimensional anisotropy of Earth's inner core. *Earth Planet. Inter.* **167,** 53–70 (2008).
3. Irving, J., Deuss, A. & Woodhouse, J. Normal mode coupling due to hemispherical anisotropic structure in Earth's inner core. *Geophys. J. Int.* **178,** 962–975 (2009).
4. Monnereau, M., Calvet, M., Margerin, L. & Souriau, A. Lopsided growth of Earth's inner core. *Science* **238,** 1014–1017 (2010).
5. Alboussière, T., Deguen, R. & Melzani, M. Melting-induced stratification above the Earth's inner core due to convective translation. *Nature* **466,** 744–747 (2010).
6. Cain, J. C., Schmitz, D. R. & Kluth, C. Eccentric geomagnetic dipole drift. *Phys. Earth Planet. Inter.* **39,** 237–242 (1985).
7. Gallet, Y., Hulot, G., Chulliat, A. & Genevey, A. Geomagnetic field hemispheric asymmetry and archaeomagnetic jerks. *Earth Planet. Sci. Lett.* **284,** 179–186 (2009).

8. Finlay, C. C. Historical variation of the geomagnetic axial dipole. *Phys. Earth Planet. Inter.* **170,** 1–14 (2008).
9. Korte, M. & Constable, C. G. Improving geomagnetic field reconstructions for 0–3 ka. *Phys. Earth Planet. Inter.* **188,** 247–259 (2011).
10. Korte, M., Constable, C. G., Donadini, F. & Holme, R. Reconstructing the Holocene geomagnetic field. *Earth Planet. Sci. Lett.* **312,** 497–505 (2011).
11. Johnson, C. & Constable, C. G. The time-averaged geomagnetic field as recorded by lava flows over the last 5 Ma. *Geophys. J. Int.* **122,** 489–519 (1995).
12. Hatekayama, T. & Kono, M. Geomagnetic field model for the last 5 My: Time-averaged field and secular variation. *Phys. Earth Planet. Inter.* **133,** 181–215 (2002).
13. Jones, C. A. in *Treatise on Geophysics* Vol. 8 (ed. Olson, P.) Ch. 4, 131–186 (Elsevier B.V., 2007).
14. Stevenson, D. J. Limits on lateral density and velocity variations in the Earth's outer core. *Geophys. J. R. Astron. Soc.* **88,** 311–319 (1987).
15. Garnero, E. J. & Helmberger, D. V. On seismic resolution of lateral heterogeneity in the Earth's outermost core. *Phys. Earth Planet. Inter.* **88,** 117–130 (1994).
16. Kustowski, B., Ekstrom, G. & Dziewonski, A. M. Anisotropic shear-wave velocity structure of the Earth's mantle: A global model. *J. Geophys. Res.* **113,** 806306 (2008).
17. Alfe, D., Gillan, M. & Price, G. Temperature and composition of the Earth's core. *Contemp. Phys.* **48,** 63–80 (2007).
18. Gubbins, D., Sreenivasan, B., Mound, J. & Rost, S. Melting of the inner core. *Nature* **473,** 361–363 (2011).
19. Sumita, I. & Olson, P. A laboratory model for convection in Earth's core driven by a thermally heterogeneous mantle. *Science* **286,** 1547–1549 (1999).
20. Aubert, J., Amit, H., Hulot, G. & Olson, P. Thermo-chemical wind flows couple Earth's inner core growth to mantle heterogeneity. *Nature* **454,** 758–762 (2008).
21. Bergman, M. I. *et al.* Grain growth and loss of texture during annealing of alloys, and the translation of Earth's inner core. *Geophys. Res. Lett.* **37,** L22313 (2010).
22. Hulot, G., Finlay, C. C., Constable, C. G., Olsen, N. & Mandea, M. The magnetic field of Planet Earth. *Space Sci. Rev.* **152,** 159–222 (2010).
23. Aubert, J. & Dumberry, M. Steady and fluctuating inner core rotation in numerical geodynamo models. *Geophys. J. Int.* **184,** 162170 (2011).
24. Zhang, N., Zhong, S., Leng, W. & Li, Z-X. A model for the evolution of the Earth's mantle structure since the Early Paleozoic. *J. Geophys. Res.* **115,** B06401 (2010).
25. Olson, P. L., Coe, R. S., Driscoll, P. E., Glatzmaier, G. A. & Roberts, P. H. Geodynamo reversal frequency and heterogeneous core–mantle boundary heat flow. *Phys. Earth Planet. Inter.* **180,** 66–79 (2010).
26. Christensen, U. & Aubert, J. Scaling properties of convection-driven dynamos in rotating spherical shells and application to planetary magnetic fields. *Geophys. J. Int.* **166,** 97–114 (2006).
27. James, R. W. & Winch, D. E. The eccentric dipole. *Pure Appl. Geophys.* **66,** 77–86 (1967).
28. Jackson, A., Jonkers, A. R. T. & Walker, M. R. Four centuries of geomagnetic secular variation from historical records. *Phil. Trans. R. Astr. Soc. Lond.* **A358,** 957–990 (2000).
29. Lesur, V., Wardinski, I., Hamoudi, M. & Rother, M. The second generation of the GFZ reference internal magnetic model: GRIMM-2. *Earth Planets Space* **62,** 765–773 (2010).

Author contributions

P.O. and R.D. jointly formulated the numerical dynamo calculations and P.O. analysed their output. R.D. formulated the offset dipole calculations and analysed the archaeomagnetic, palaeomagnetic and geomagnetic data to produce the dipole offset histories. P.O. and R.D. jointly wrote the paper.

Additional information

The authors declare no competing financial interests. Supplementary information accompanies this paper on www.nature.com/naturegeoscience. Reprints and permissions information is available online at www.nature.com/reprints. Correspondence and requests for materials should be addressed to P.O.